OPEN ACCESS

atoms

Article

Electron Impact Excitation and Dielectronic Recombination of Highly Charged Tungsten Ions

Zhongwen Wu, Yanbiao Fu, Xiaoyun Ma, Maijuan Li, Luyou Xie, Jun Jiang and Chenzhong Dong *

Key Laboratory of Atomic and Molecular Physics & Functional Materials of Gansu Province,
College of Physics and Electronic Engineering, Northwest Normal University, Lanzhou 730070, China;
E-Mails: wuzhongwen05@126.com (Z.W.); fuyb@nwnu.edu.cn (Y.F.); mxyun_2006@126.com (X.M.);
westmaijuan2@163.com (M.L.); xiely@nwnu.edu.cn (L.X.); phyjiang@yeah.net (J.J.)

* Author to whom correspondence should be addressed; E-Mail: dongcz@nwnu.edu.cn.

Academic Editors: Alfred Müller, Bastiaan J. Braams, Peter Beiersdorfer and Yuri Ralchenko

Abstract: Electron impact excitation (EIE) and dielectronic recombination (DR) of tungsten ions are basic atomic processes in nuclear fusion plasmas of the International Thermonuclear Experimental Reactor (ITER) tokamak. Detailed investigation of such processes is essential for modeling and diagnosing future fusion experiments performed on the ITER. In the present work, we studied total and partial electron-impact excitation (EIE) and DR cross-sections of highly charged tungsten ions by using the multiconfiguration Dirac–Fock method. The degrees of linear polarization of the subsequent X-ray emissions from unequally-populated magnetic sub-levels of these ions were estimated. It is found that the degrees of linear polarization of the same transition lines, but populated respectively by the EIE and DR processes, are very different, which makes diagnosis of the formation mechanism of X-ray emissions possible. In addition, with the help of the flexible atomic code on the basis of the relativistic configuration interaction method, DR rate coefficients of highly charged W^{37+} to W^{46+} ions are also studied, because of the importance in the ionization equilibrium of tungsten plasmas under running conditions of the ITER.

Keywords: electron impact excitation; dielectronic recombination; highly charged tungsten ions; DR rate coefficients; degree of linear polarization

1. Introduction

Owing to its physical properties of high melting temperature, excellent thermal conductivity, low sputtering rate and low affinity for tritium [1,2], tungsten has been used as a plasma-facing material in several magnetic confinement fusion facilities [3–6] and is planned to be used in the divertor region having the highest heat load in the International Thermonuclear Experimental Reactor (ITER) tokamak [7]. However, inevitably, tungsten appears as an intrinsic impurity in fusion plasmas, which results in some severe problems due to its high radiation efficiency. The radiated X-ray emissions from excited tungsten lead to substantial plasma cooling that has to be well controlled in order to maintain conditions for nuclear fusions [8–13]. Therefore, it is important to know the atomic properties of tungsten in plasma under the conditions ranging from the cold temperature ($\simeq$ 1 eV) of near-wall plasma to the approximate 20 keV electron temperature expected in the plasma core region. X-ray emissions from highly charged tungsten ions can be used as diagnostic probes to reflect the information on the fusion plasmas. W^{46+}–W^{42+} ions are arranged in a filled M-shell structure that are expected to be present over a wide range of electron temperatures in plasmas. The radiated X-rays from strong M-band ($nf \to 3d$) atomic transitions have great significance in that they are suitable for fusion plasma modeling and diagnostics, since the radiations involving the $3d$ subshell are very intense [13]. Because of that, these charge states of tungsten are selected to study X-ray polarization in the present work.

Up to now, the atomic properties of tungsten have been extensively studied experimentally by using plasma devices, beams and trapped ions and theoretically by atomic structure and scattering calculations. For example, charge state distribution in plasmas, X-ray emission spectra and transition properties following electron-impact excitation (EIE) and ionization, as well as dielectronic recombination (DR) processes have been performed. An overview of the photoionization, electron-impact ionization, as well as electron-ion recombination of low to moderately-charged tungsten ions was reported very recently, together with a critical assessment of the methods and results [14]. Extreme-ultraviolet (EUV) spectra from a variety of tungsten ions have been recorded at the electron beam ion trap and the Axially Symmetric Divertor EXperiment (ASDEX) Upgrade tokamak facilities [15–21]. The majority of these spectra have been identified and assigned to $nf \to 3d$ (n = 4, 5, 6) and $4d \to 3p$ atomic transitions mostly by performing fully-relativistic *ab initio* calculations [22–25]. Besides atomic structure and spectra, the dynamical processes of tungsten ions were also investigated for the purpose of X-ray diagnostics and simulation, such as electron-impact ionization [26], electron-impact excitation [27,28] and dielectronic recombination [29]. However, to the best of our knowledge, there are few work about the linear polarization of tungsten X-ray emissions in ITER fusion plasmas. Since angle-resolved observables, such as linear polarization and angular distribution, are much more sensitive to various atomic effects and physical variables than the total (angle-averaged) decay rates of X-ray emissions, the angle-resolved studies of X-rays have been used to extract a variety of physical effects in the last few decades [30–36]. For those strong X-ray emissions from tungsten ions, they are hardly affected by the radiative damping caused by additional atomic excitation processes [27] and, thus, are relatively clean atomic radiations, which could be used to study the angle-resolved observables to reveal the population mechanism of excited levels [37,38] and perhaps to reflect plasma conditions. In the present work, linear polarization of tungsten X-ray emissions from strong $nf \to 3d$ (n = 4, 5, 6) radiative transitions

following electron-impact excitation and resonant electron capture (REC) of W^{42+} to W^{46+} ions is studied theoretically.

Moreover, DR has been known as one of the important recombination processes, which plays dominant roles in the ionization equilibrium of various plasmas. Triggered by this, much work on the DR process and the rate coefficients of tungsten ions has been done, both theoretically and experimentally [39–50]. For example, the Atomic Data and Analysis Structure (ADAS) database is currently used for modeling plasmas in the community [7,42,51,52]. The computations of DR rate coefficients from the ADAS are based on the generalized collisional-radiative framework [53] and the semiempirical Burgess formulas [54]. Although many experiments on spectral emissions from tungsten have been carried out, especially at the ASDEX Upgrade tokamak [2–4,7,17,51], the first measurement on DR rate coefficients of tungsten ions was performed just recently for W^{20+} using the technique of the electron-ion merged beam at the heavy ion storage ring [39]. A big discrepancy with a factor of four was found between the measured and calculated rate coefficients from the ADAS database, which was attributed to the neglect of DR-associated fine-structure excitations of W^{20+} in the calculations [39]. Further intermediate-coupling calculations with all important single-electron excitations reduced the discrepancy to a factor of three at an electron temperature of 1 eV and to a much better 50%–30% among 100–300 eV [42]. Very recently, other theoretical methods, such as the configuration-average distorted-wave method [41], the statistical theory of resonant multielectron recombination [43,44] and the Breit–Wigner partitioned method [40], were further developed to calculate DR rate coefficients. These methods could produce results that agree reasonably well with the experimental findings. Apart from DR, radiative recombination (RR) is another non-negligible recombination process in which the fusion community is interested. For example, Trzhaskovskaya *et al.* calculated in great detail RR cross-sections and rate coefficients, as well as radiated power loss rate coefficients for a wide range of tungsten ions W^{14+}–W^{71+} [55–58]. With the purpose of assisting the simulation of the ionization equilibrium of tungsten plasmas, DR rate coefficients of W^{37+} to W^{46+} ions are studied, as well, in the present work.

The paper is structured as follows. In the next section, theoretical methods for calculating partial EIE and DR cross-sections, linear polarization of X-ray emissions and DR rate coefficients are described. In Section 3, we discuss the calculated partial cross-sections and DR rate coefficients and especially compare the linear polarization of X-rays for both cases of EIE and DR. Finally, a few conclusions of the present work are given in Section 4.

2. Theoretical Background

2.1. Electron Impact Excitation and Dielectronic Recombination Cross-Sections

In the present work, a recently-developed computational code, REIE06 [38,59], is utilized to calculate electron-impact excitation cross-sections that is based on the fully-relativistic distorted-wave (RDW) method. In this method, the partial electron-impact excitation cross-section from an initial $\beta_i J_i M_i$ state to a final $\beta_f J_f M_f$ state of ions is given by [60,61]:

$$
\begin{aligned}
\sigma_{\varepsilon_i}(\beta_i J_i M_i - \beta_f J_f M_f) = \frac{2\pi a_0^2}{k_i^2} \cdot \sum_{l_i, l_i', j_i, j_i', m_{s_i}, l_f, j_f, m_f} \sum_{J, J', M} i^{(l_i - l_{i'}')} [(2l_i + 1)(2l_i' + 1)]^{1/2} \\
\times \exp[i(\delta_{\kappa_i} - \delta_{\kappa_{i'}})] \, C(l_i \tfrac{1}{2} m_{l_i} m_{s_i}; j_i m_i) \, C(l_i' \tfrac{1}{2} m_{l_i'} m_{s_i}; j_i' m_i) \\
\times C(J_i j_i M_i m_i; JM) \, C(J_i j_i' M_i m_i; J'M) \, C(J_f j_f M_f m_f; JM) \\
\times C(J_f j_f M_f m_f; J'M) \, R(\gamma_i, \gamma_f) \, R(\gamma_i', \gamma_f').
\end{aligned}
\tag{1}
$$

Here, the subscripts i and f refer to the initial and final states, respectively; ε_i is the incident electron energy in the Rydberg; a_0 is the Bohr radius; Cs are Clebsch–Gordan coefficients; $\gamma_i = \varepsilon_i l_i j_i \beta_i J_i J M$ and $\gamma_f = \varepsilon_f l_f j_f \beta_f J_f J M$; J and M represent the total angular momentum and its z component for the impact system, *i.e.*, target ion plus free electron; β represents all additional quantum numbers required to specify the initial and final states of the target ion in addition to its total angular momentum J and z component M; $m_{s_i}, l_i, j_i, m_{l_i}$ and m_i are the spin, orbital angular momentum, total angular momentum and its z component quantum numbers, respectively, for the incident electron e_i; δ_{κ_i} is the phase factor for the continuum electron; κ is the relativistic quantum number, which is related to the orbital and total angular momentum l and j; k_i is the relativistic wave number of the incident electron and given by $k_i^2 = \varepsilon_i(1 + \alpha^2 \varepsilon_i/4)$ with the fine-structure constant α. R's denote the electron-impact excitation matrix elements, which can be represented as:

$$
R(\gamma_i, \gamma_f) = \langle \Psi_{\gamma_f} | \sum_{p, q, p<q}^{N+1} (V_{Coul} + V_{Breit}) | \Psi_{\gamma_i} \rangle,
\tag{2}
$$

in which, besides the leading Coulomb interaction, the Breit interaction is also taken into account; Ψ_{γ_i} and Ψ_{γ_f} are the antisymmetric $N + 1$ electron wavefunctions for the initial and final states of the impact system. In the present calculations, the target state wavefunctions are generated with the use of the atomic structure package GRASP92 [62] based on the multiconfiguration Dirac–Fock (MCDF) method, and the continuum electron wavefunctions are produced with the component COWF of the RATIP package [63] by solving the coupled Dirac equation in which the exchange effect between the bound and continuum electrons is considered. To obtain accurate atomic energy levels and wavefunctions of the initial and final states, the contribution of the quantum electrodynamics effect has been taken into account. Additionally, the partial-waves of the free electron up to $\kappa = 50$ are included to ensure convergence of cross-sections in the present calculation.

For initially randomly-oriented target ions, the case of interest here, one can average over initial magnetic sub-levels M_i of the target ion and then obtain the cross-section for electron-impact excitation to a specific final magnetic sub-level M_f,

$$
\sigma_{\varepsilon_i}(\beta_i J_i - \beta_f J_f M_f) = \frac{1}{2J_i + 1} \sum_{M_i} \sigma_{\varepsilon_i}(\beta_i J_i M_i - \beta_f J_f M_f).
\tag{3}
$$

The same excited state populated in the electron-impact excitation process perhaps can also be produced in the dielectronic recombination process. In this case, we are interested in the resonant capture cross-section from an initial state i to an final state i, which can be given as follows if the capture electrons are spin-unpolarized: [61]

$$\sigma_{\varepsilon_i}^{cap}(\beta_i J_i M_i - \beta_f J_f M_f) = \frac{2\pi a_0^2}{k_{i^2}} \cdot \sum_{l_i, l_i', j_i, j_i', m_{s_i}} i^{(l_i - l_i')} [(2l_i + 1)(2l_i' + 1)]^{1/2} \exp[i(\delta_{\kappa_i} - \delta_{\kappa_i'})]$$

$$\times C(l_i \frac{1}{2} 0 m_{s_i}; j_i m_i) \, C(l_i' \frac{1}{2} 0 m_{s_i}; j_i' m_i) \, C(J_i j_i M_i m_i; J_f M_f)$$

$$\times C(J_i j_i' M_i m_i; J_f M_f) \, R(\gamma_f, \gamma_i) \, R(\gamma_f', \gamma_i') \, \delta(\varepsilon_i - \varepsilon_{if}), \tag{4}$$

where the delta function $\delta(\varepsilon_i - \varepsilon_{if})$ guarantees the resonance condition of the dielectronic recombination; R's denote the resonant capture matrix elements. Similarly, the partial resonant capture cross-section from an initial level to a particular final magnetic substate can be easily obtained by using the same route as in the case of the electron impact excitation.

2.2. Degree of Linear Polarization of Radiated X-ray Emissions

Experimentally, the degree of linear polarization for radiated X-ray emissions is defined as follows if the scattered electron is not detected [64]:

$$P = \frac{I_\parallel - I_\perp}{I_\parallel + I_\perp}, \tag{5}$$

where $I_\parallel$ and $I_\perp$ denote the intensities of emitted X-ray photons with the electric vectors parallel and perpendicular to the direction of the incident electron, respectively.

In order to calculate the degree of linear polarization, we use the density matrix theory [65,66] to derive its computational formula, the particular form of which actually depends on the total angular momentum of the initial and final atomic levels related to radiated X-ray emissions. Take the $J_i = 1 \rightarrow J_f = 0$ and $J_i = 3/2 \rightarrow J_f = 1/2$ radiative transitions of our interest for example; the degree of linear polarization for corresponding X-ray emissions is given by [37,67]:

$$P = \frac{\sigma_0 - \sigma_1}{\sigma_0 + \sigma_1}, \tag{6}$$

$$P = \frac{3(\sigma_{1/2} - \sigma_{3/2})}{5\sigma_{1/2} + 3\sigma_{3/2}}. \tag{7}$$

If we assume that the electron-impact excitation process is the dominant mechanism for populating upper magnetic substates, σ_0 and σ_1 denote the partial cross-sections for electron-impact excitation from the ground level to the magnetic substates $M_f = 0$ and $M_f = 1$ of the excited level, respectively. In contrast, if the dielectronic recombination process is the leading population mechanism for upper magnetic substates, σ_0 and σ_1 are the partial capture cross-sections from the ground level to the magnetic substates $M_f = 0$ and $M_f = 1$ of the resonant doubly-excited level, respectively. Furthermore, $\sigma_{1/2}$ and $\sigma_{3/2}$ have similar meaning in both cases of electron-impact excitation and dielectronic recombination.

2.3. Dielectronic Recombination Rate Coefficients

Apart from degree of linear polarization of X-ray emissions following electron-impact excitation and dielectronic recombination, DR rate coefficients of tungsten ions are also studied in the present work.

In the isolated-resonance approximation, if we assume that the electron velocity obeys the Maxwellian distribution in plasmas, DR rate coefficients can be given by [68]:

$$\alpha^{DR}(kT_e) \,=\, \Big(\frac{2\pi\hbar^2}{m_e kT_e}\Big)^{3/2} \frac{g_j}{2g_i}\, A_{ji}^a\, B_{j,f}^r\, \exp\Big(-\frac{E_{ij}}{kT_e}\Big). \tag{8}$$

Here, kT_e is the electron temperature, $\hbar$ is the reduced Planck's constant, m_e is the electron mass, g_i and g_j denote the statistical weights of the initial and intermediate ionic states, respectively, and E_{ij} represents the resonance energy. Moreover, $B_{j,f}^r$ refers to the so-called radiative branching ratio and is defined in terms of the Auger decay rate A_{ji}^a and the radiative decay rate A_{jf}^r as follows:

$$B_{j,f}^r \,=\, \frac{A_{jf}^r}{\sum_{f'} A_{jf'}^r + \sum_{i'} A_{ji'}^a}, \tag{9}$$

where the summations over f' and i' run through all of the possible radiative and Auger final states, respectively. The Auger and radiative decay rates are given respectively by:

$$A_{ji}^a \,=\, \frac{2\pi}{\hbar} \Big| \langle \Psi_{i\varepsilon_i} | \sum_{p,q,\,p<q} (V_{\mathrm{Coul}} + V_{\mathrm{Breit}}) | \Psi_j \rangle \Big|^2, \tag{10}$$

$$A_{jf}^r \,=\, \frac{4e^2\omega}{3c^3 g_j \hbar} \Big| \langle \Psi_f | T^{(t)} | \Psi_j \rangle \Big|^2. \tag{11}$$

Here, $\Psi_{i\varepsilon_i}$ denotes the atomic state function (ASF) of the combined system consisting of the initial bound state i and a free electron with kinetic energy ε_i; Ψ_j and Ψ_f the ASFs of the bound states j and f, respectively; V_{Coul} and V_{Breit} the Coulomb and Breit operators; and the summation runs over all pairs of electrons. Moreover, e and c have their usual meaning; ω denotes the photon energy; $T^{(t)}$ represents the radiative tensor operator with the multipoles t; and in the present calculations, we consider just dominant electric-dipole (E1) transitions, *i.e.*, $t = 1$. As seen from Equations (8) and (9), the computation of DR rate coefficients can be traced back to the Auger A_{ji}^a and the radiative A_{jf}^r decay rates of associated DR process. In order to calculate these decay rates, we here use the flexible atomic code (FAC) that is based on the relativistic configuration-interaction method [69,70]. In this method, an atomic state function is approximated by a linear combination of configuration state functions (CSFs) with the same symmetries. In addition, the CSFs are constructed as antisymmetrized products of a common basis set of orthonormal orbits that is optimized with regards to the Dirac–Coulomb Hamiltonian.

3. Results and Discussion

In the present work, we studied the linear polarization of X-ray emissions from unequally-populated magnetic sub-levels following the EIE and REC of highly charged tungsten ions. To do this, we firstly calculated the corresponding total and magnetic sub-level cross-sections. In addition, DR rate coefficients of highly charged tungsten ions have been also studied due to the importance in modeling the ionization equilibrium of tungsten plasmas.

3.1. Excitation Energies and Electron-Impact Excitation Cross-Sections

To ensure the validity of our results, the presently calculated transition energies for the $3d \to nf$ ($n =$ 4, 5, 6) excitations of W^{46+}–W^{42+} ions are given in Table 1 together with other available theoretical and experimental results [71–73]. A good agreement among them has been found within the experimental errors. The relative differences are expected to be less than 0.07% for W^{46+} and 0.17% for W^{45+}. For other lower charged tungsten ions, the deviations are also kept within 0.3%. For example, the present energy is 2111.59 eV for the $3d_{5/2} \to 4f_{7/2}$ excitation of W^{46+}, compared to the experimental result 2112.2 ± 3.0 eV and other theoretical values 2112.57 eV and 2110.20 eV. For illustrating further the reliability of the present calculations, in addition, total EIE cross-sections for the $3d_{5/2} \to 4f_{7/2}$ and $3d_{3/2} \to 4f_{5/2}$ excitations of W^{46+} ions are plotted in Figure 1 compared to the previous RDW results from Das *et al.* [72] and Zhang *et al.* [74], as well as the relativistic *R*-matrix results from Ballance *et al.* [27]. In all of these calculations, the contribution of the Breit interaction is taken into account, which has been proven to be very important [32,36,37,75]. As seen from the figure, the present cross-sections are a little bit smaller than other ones. Nevertheless, the results from different calculations are in good accord with each other, especially for the $3d_{5/2} \to 4f_{7/2}$ excitation. Since the subsequent radiative transitions from these two excited levels to the ground state have the largest decay rates, the resonant contribution to these two excitations remains very small, and thus, the effect of the radiative damping caused by resonant excitations is negligible, as demonstrated in [27]. Under such an analysis, the discrepancy among different curves could be attributed mostly to the treatment of bound-state wavefunctions and energy levels before and after electron-impact excitation, *i.e.*, atomic configurations considered to expand the relevant atomic state functions.
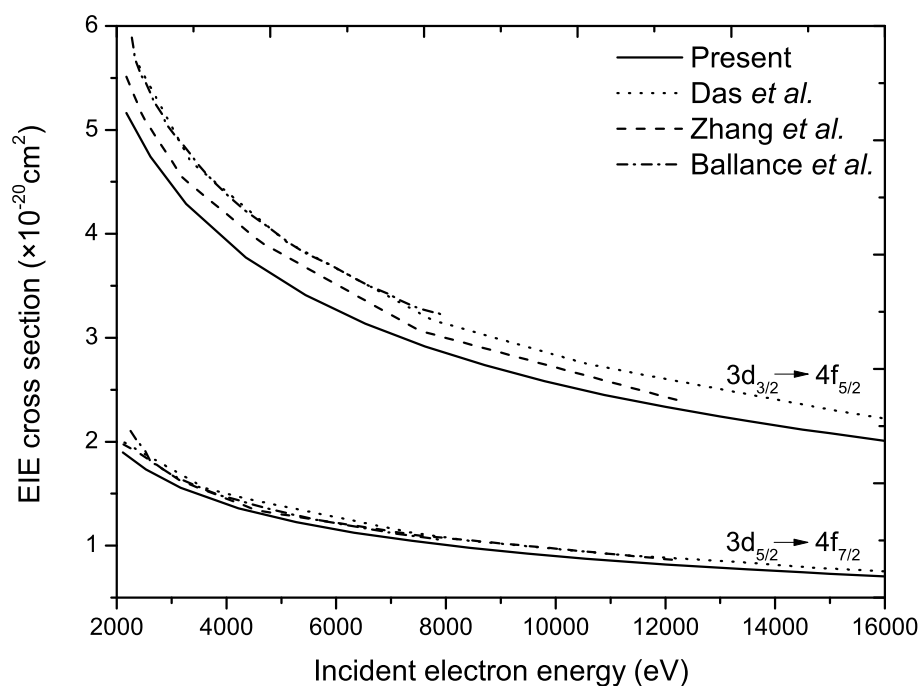
Figure 1. The presently calculated total cross-sections for the $3d_{5/2} \to 4f_{7/2}$ and $3d_{3/2} \to 4f_{5/2}$ electron-impact excitations of W^{46+} ions as a function of incident electron energy together with other available results from Das *et al.* [72], Zhang *et al.* [74] and Ballance *et al.* [27].
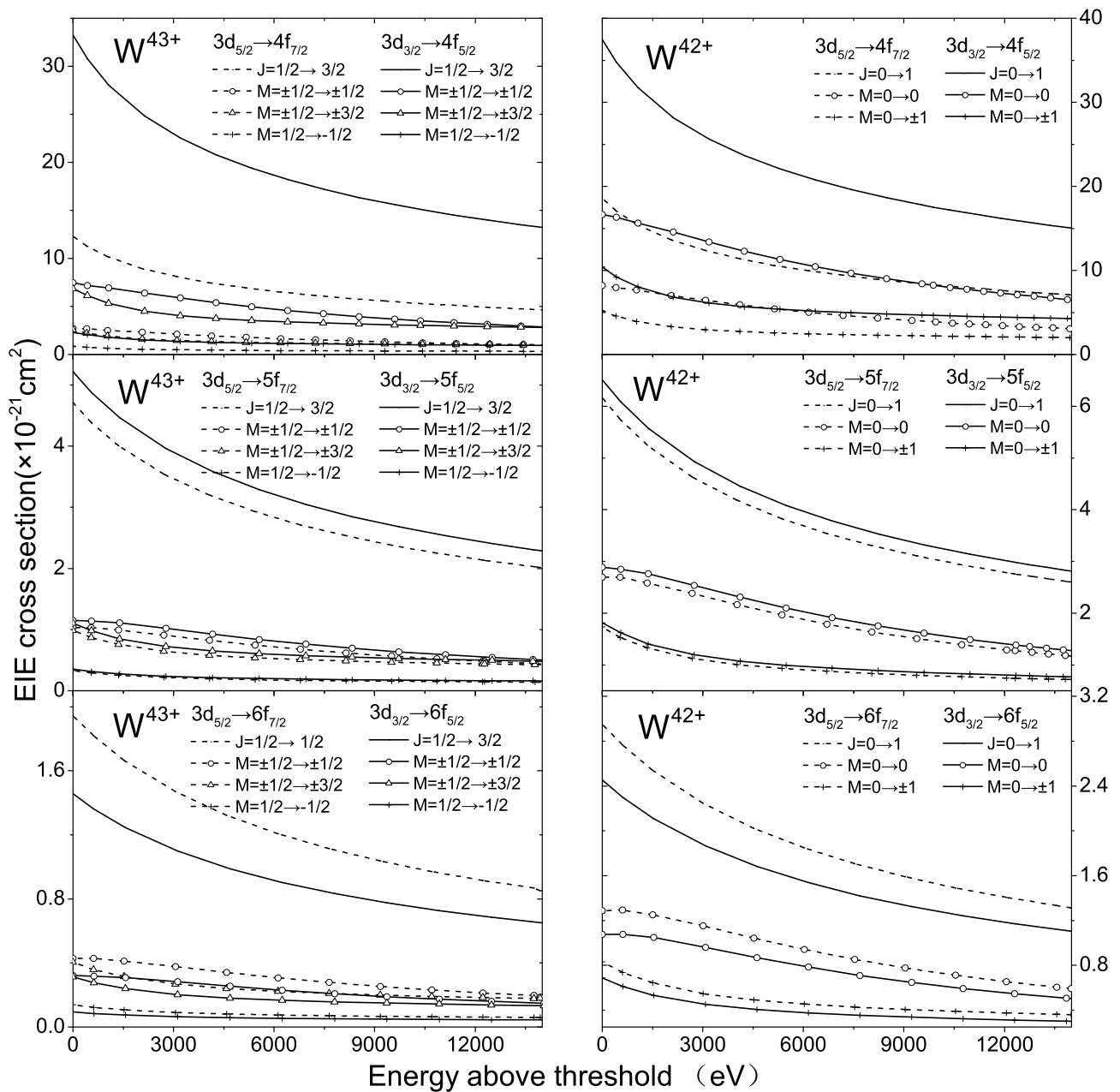
Table 1. The presently calculated excitation energies (eV) for electron-impact excitations $3d \to nf$ (n = 4, 5, 6) of W^{46+}–W^{42+} ions together with other available theoretical and experimental results. Note that closed inner-subshells have been omitted from the upper and lower levels for the sake of brevity. Experimental errors are given in the parenthesis.

Ions	Upper Level → Lower level	Present	Theo. [71]	Theo. [72]	Exp. [73]
W^{46+}	$(3d_{5/2}^{-1}4f_{7/2})_{J=1} \to (3d^{10})_{J=0}$	2111.59	2112.57	2110.20	2112.2(3)
	$(3d_{3/2}^{-1}4f_{5/2})_{J=1} \to (3d^{10})_{J=0}$	2179.97	2181.36	2178.88	2179.7(4)
	$(3d_{5/2}^{-1}5f_{7/2})_{J=1} \to (3d^{10})_{J=0}$	2814.39		2812.61	2816.1(3)
	$(3d_{3/2}^{-1}5f_{5/2})_{J=1} \to (3d^{10})_{J=0}$	2876.70		2874.99	2878.2(3)
	$(3d_{5/2}^{-1}6f_{7/2})_{J=1} \to (3d^{10})_{J=0}$	3194.47		3193.12	3196.8(3)
	$(3d_{3/2}^{-1}6f_{5/2})_{J=1} \to (3d^{10})_{J=0}$	3257.73		3256.57	3259.9(3)
W^{45+}	$(3d_{5/2}^{-1}4s4f_{7/2})_{J=3/2} \to (3d^{10}4s)_{J=1/2}$	2098.36	2094.9	2097.57	2094.8(5)
	$(3d_{3/2}^{-1}4s4f_{5/2})_{J=3/2} \to (3d^{10}4s)_{J=1/2}$	2166.84	2169.8	2166.07	
	$(3d_{5/2}^{-1}4s5f_{7/2})_{J=3/2} \to (3d^{10}4s)_{J=1/2}$	2782.97	2783.1	2781.62	
	$(3d_{3/2}^{-1}4s5f_{5/2})_{J=3/2} \to (3d^{10}4s)_{J=1/2}$	2843.69	2844.7	2843.41	
	$(3d_{5/2}^{-1}4s6f_{7/2})_{J=3/2} \to (3d^{10}4s)_{J=1/2}$	3149.21	3151.9	3149.69	
	$(3d_{3/2}^{-1}4s6f_{5/2})_{J=3/2} \to (3d^{10}4s)_{J=1/2}$	3211.78	3214.7	3212.49	3215.8(5)
W^{44+}	$(3d_{5/2}^{-1}4f_{7/2})_{J=1} \to (3d^{10}4s^2)_{J=0}$	2085.38	2082.6	2084.35	2082.2(4)
	$(3d_{3/2}^{-1}4f_{5/2})_{J=1} \to (3d^{10}4s^2)_{J=0}$	2152.70	2159.0	2152.04	
	$(3d_{5/2}^{-1}5f_{7/2})_{J=1} \to (3d^{10}4s^2)_{J=0}$	2751.51	2750.2	2749.98	2750.3(10)
	$(3d_{3/2}^{-1}5f_{5/2})_{J=1} \to (3d^{10}4s^2)_{J=0}$	2813.45	2811.6		
	$(3d_{5/2}^{-1}6f_{7/2})_{J=1} \to (3d^{10}4s^2)_{J=0}$	3104.45	3107.9	3105.54	3107.8(5)
	$(3d_{3/2}^{-1}6f_{5/2})_{J=1} \to (3d^{10}4s^2)_{J=0}$	3167.36	3171.0	3168.62	3171.2(6)
W^{43+}	$(3d_{5/2}^{-1}4p_{1/2}4f_{7/2})_{J=3/2} \to (3d^{10}4p_{1/2})_{J=1/2}$	2067.96			
	$(3d_{3/2}^{-1}4p_{1/2}4f_{5/2})_{J=3/2} \to (3d^{10}4p_{1/2})_{J=1/2}$	2136.12	2140.3		
	$(3d_{5/2}^{-1}4p_{1/2}5f_{7/2})_{J=3/2} \to (3d^{10}4p_{1/2})_{J=1/2}$	2715.49	2718.1		
	$(3d_{3/2}^{-1}4p_{1/2}5f_{5/2})_{J=3/2} \to (3d^{10}4p_{1/2})_{J=1/2}$	2780.92	2781.1		
	$(3d_{5/2}^{-1}4p_{1/2}6f_{7/2})_{J=3/2} \to (3d^{10}4p_{1/2})_{J=1/2}$	3060.51	3062.1		
	$(3d_{3/2}^{-1}4p_{1/2}6f_{5/2})_{J=3/2} \to (3d^{10}4p_{1/2})_{J=1/2}$	3124.77	3126.7		
W^{42+}	$(3d_{5/2}^{-1}4p_{1/2}^2 4f_{7/2})_{J=1} \to (3d^{10}4p_{1/2}^2)_{J=0}$	2054.00			
	$(3d_{3/2}^{-1}4p_{1/2}^2 4f_{5/2})_{J=1} \to (3d^{10}4p_{1/2}^2)_{J=0}$	2119.98			
	$(3d_{5/2}^{-1}4p_{1/2}^2 5f_{7/2})_{J=1} \to (3d^{10}4p_{1/2}^2)_{J=0}$	2683.09			
	$(3d_{3/2}^{-1}4p_{1/2}^2 5f_{5/2})_{J=1} \to (3d^{10}4p_{1/2}^2)_{J=0}$	2748.89			
	$(3d_{5/2}^{-1}4p_{1/2}^2 6f_{7/2})_{J=1} \to (3d^{10}4p_{1/2}^2)_{J=0}$	3016.27			
	$(3d_{3/2}^{-1}4p_{1/2}^2 6f_{5/2})_{J=1} \to (3d^{10}4p_{1/2}^2)_{J=0}$	3080.31			

Up to now, we are ready to study electron-impact excitation of highly charged tungsten ions. In this part, we focus on the excitations $3d_{3/2} \to nf_{5/2}$ and $3d_{5/2} \to nf_{7/2}$ (n = 4, 5, 6) of W^{46+}–W^{42+} ions that can subsequently give rise to very strong X-ray emissions. Since $W^{42+,44+,46+}$ ions have a similar shell structure and this is also true for $W^{43+,45+}$ ions, only W^{43+} and W^{42+} ions are taken here as examples. In Figure 2, the calculated total and magnetic sub-level cross-sections for the excitations $3d \to nf$ (n = 4, 5, 6) of W^{42+} and W^{43+} ions are given as a function of incident electron energy. Take the excitations $3d_{3/2} \to 4f_{5/2}$ and $3d_{5/2} \to 4f_{7/2}$ of W^{42+} for example; the total cross-sections decrease with increasing incident electron energy, and it behaves more sensitively to less-energetic electron collisions than to

energetic ones. With respect to the magnetic sub-levels, the partial cross-sections for electron-impact excitation to the $M_f = 0$ substate are significantly larger than the ones to the $M_f = \pm 1$ states. This indicates that the magnetic sub-level $M_f = 0$ is preferentially populated in the electron-impact excitation process. Similarly, the same characteristics can be summarized for the $3d \to 5f$ and $3d \to 6f$ excitations. In addition, for W^{43+} ions, the cross-sections for electron-impact excitations to the $M_f = \pm 1/2$ substates are larger than the ones to the $M_f = \pm 3/2$ and $M_f = \mp 1/2$ substates, and the magnetic sub-level cross-sections for the $M_f = \mp 1/2$ substates are much smaller at all given incident electron energies. Since the magnetic sub-level cross-sections for excitation to the $M_f = \mp 3/2$ substates are negligibly smaller than others by four orders of magnitude, they are not plotted in the figure.

Figure 2. The presently calculated total and magnetic sub-level cross-sections for electron-impact excitations $3d_{3/2} \to nf_{5/2}$ and $3d_{5/2} \to nf_{7/2}$ (n = 4, 5, 6) of W^{43+} (left panel) and W^{42+} (right panel) ions as a function of incident electron energy.

### 3.2. Resonant Energies and Resonant Electron Capture Cross-Sections

Besides the electron-impact excitation processes, the resonant electron capture can also populate those excited levels that subsequently give rise to the same X-ray emissions. In Table 2, for W^{45+}–W^{42+} final ions, we identify some of possible population processes and show the associated resonant energies, as well as total and magnetic sub-level REC cross-sections. As seen from the table, only the doubly-excited $3d^{-1}4lnf$ ($l = s, p$; $n = 5, 6$) levels are considered compared to the case of the electron-impact excitations. The $3d^{-1}4s4f$ and $3d^{-1}4p4f$ excited levels are not included, since they are not auto-ionizing states of W^{45+}–W^{42+} final ions. For a given n ($n = 5, 6$), the $nf_{5/2}$ resonant energies are greater than the $nf_{7/2}$ ones, and the differences are approximately 63 eV and 65 eV for each n, respectively. Moreover, $\sigma_{M=i \to f}$ in the table represents magnetic sub-level cross-sections for REC to the M_f final substate from the M_i initial substate. The same as in electron-impact excitation, the magnetic sub-levels here are not populated statistically. Note that the REC channels with $|M_i - M_f| > 1$ are forbidden due to selection rules of angular momentum as shown by $\sigma_{M=\pm 1/2 \to \mp 1} = 0$ and $\sigma_{M=0 \to \pm 3/2} = 0$. Finally, the resonant electron capture processes give rise to larger total and magnetic sub-level cross-sections, compared to the case of electron-impact excitations at almost all given incident electron energies.

Table 2. The presently calculated resonant energies (eV), as well as total and magnetic sub-level cross-sections (10^{-20} cm^2) for resonant nf ($n = 5, 6$) electron captures of final W^{45+}–W^{42+} ions. Note that closed inner-subshells have been omitted from the initial and final levels for the sake of brevity.

Ions	Initial Level → Final Level	$\triangle E$	Magnetic Sub-level CS$\sigma_{M=i \to f}$			Total CS
W^{45+}			$\sigma_{0 \to \pm 1/2}$	$\sigma_{0 \to \pm 3/2}$		
	$(3d^{10})_{J=0} \to (3d^{-1}_{5/2}4s5f_{7/2})_{J=3/2}$	363.89	21.1	0		42.2
	$(3d^{10})_{J=0} \to (3d^{-1}_{3/2}4s5f_{5/2})_{J=3/2}$	425.39	28.0	0		56.0
	$(3d^{10})_{J=0} \to (3d^{-1}_{5/2}4s6f_{7/2})_{J=3/2}$	732.42	5.12	0		10.2
	$(3d^{10})_{J=0} \to (3d^{-1}_{3/2}4s6f_{5/2})_{J=3/2}$	794.99	5.97	0		11.9
W^{44+}			$\sigma_{\pm 1/2 \to 0}$	$\sigma_{\pm 1/2 \to \mp 1}$	$\sigma_{\pm 1/2 \to \pm 1}$	
	$(3d^{10}4s)_{J=1/2} \to (3d^{-1}_{5/2}5f_{7/2})_{J=1}$	398.44	11.8	0	0.26	12.1
	$(3d^{10}4s)_{J=1/2} \to (3d^{-1}_{3/2}5f_{5/2})_{J=1}$	460.17	12.9	0	1.19	14.1
	$(3d^{10}4s)_{J=1/2} \to (3d^{-1}_{5/2}6f_{7/2})_{J=1}$	754.40	3.02	0	0.10	3.12
	$(3d^{10}4s)_{J=1/2} \to (3d^{-1}_{3/2}6f_{5/2})_{J=1}$	817.30	2.79	0	0.34	3.16
W^{43+}			$\sigma_{0 \to \pm 1/2}$	$\sigma_{0 \to \pm 3/2}$		
	$(3d^{10}4s^2)_{J=0} \to (3d^{-1}_{5/2}4p_{1/2}5f_{7/2})_{J=3/2}$	513.23	1.06	0		2.12
	$(3d^{10}4s^2)_{J=0} \to (3d^{-1}_{3/2}4p_{1/2}5f_{5/2})_{J=3/2}$	575.84	0.64	0		1.28
	$(3d^{10}4s^2)_{J=0} \to (3d^{-1}_{5/2}4p_{1/2}6f_{7/2})_{J=3/2}$	856.78	0.10	0		0.20
	$(3d^{10}4s^2)_{J=0} \to (3d^{-1}_{3/2}4p_{1/2}6f_{5/2})_{J=3/2}$	921.03	0.01	0		0.02
W^{42+}			$\sigma_{\pm 1/2 \to 0}$	$\sigma_{\pm 1/2 \to \mp 1}$	$\sigma_{\pm 1/2 \to \pm 1}$	
	$(3d^{10}4p_{1/2})_{J=1/2} \to (3d^{-1}_{5/2}4p^2_{1/2}5f_{7/2})_{J=1}$	536.81	2.53	0	1.11	3.64
	$(3d^{10}4p_{1/2})_{J=1/2} \to (3d^{-1}_{3/2}4p^2_{1/2}5f_{5/2})_{J=1}$	598.89	3.00	0	2.08	5.08
	$(3d^{10}4p_{1/2})_{J=1/2} \to (3d^{-1}_{5/2}4p^2_{1/2}6f_{7/2})_{J=1}$	868.14	0.69	0	0.56	1.24
	$(3d^{10}4p_{1/2})_{J=1/2} \to (3d^{-1}_{3/2}4p^2_{1/2}6f_{5/2})_{J=1}$	931.56	0.68	0	0.85	1.53

3.3. Degrees of Linear Polarization of Subsequently Radiated X-Ray Emissions

Once we obtain the magnetic sub-level cross-sections (*i.e.*, the relative populations) of excited levels, the degree of linear polarization of X-ray emissions radiated from these levels can be calculated by using Equations (6) and (7). In Figure 3, we show the degrees of linear polarization of X-ray emissions following the $3d \rightarrow nf$ ($n = 4, 5, 6$) electron-impact excitations of W^{43+} and W^{42+} ions just as examples. Again, the results for W^{46+}–W^{44+} ions are not given here owing to very similar characteristics shown in the figure. As seen clearly, the X-ray emissions are strongly linearly polarized and possess positive degrees of polarization, which means that these X-rays are preferentially emitted perpendicular to the direction of incident electrons. Besides, these X-ray emissions have very similar polarization behaviors with respect to incident electron energy. As the incident electrons move more energetically, at first, the X-ray emissions become more linearly polarized up to a maximum degree at approximately 2.5-times their excitation thresholds, and then, a depolarization of X-ray emissions occurs at higher electron energies. For example, such a maximum degree reaches 0.20 and 0.37 for the $3d_{5/2} \rightarrow 4f_{7/2}$ excitations of W^{43+} and W^{42+} ions, respectively.
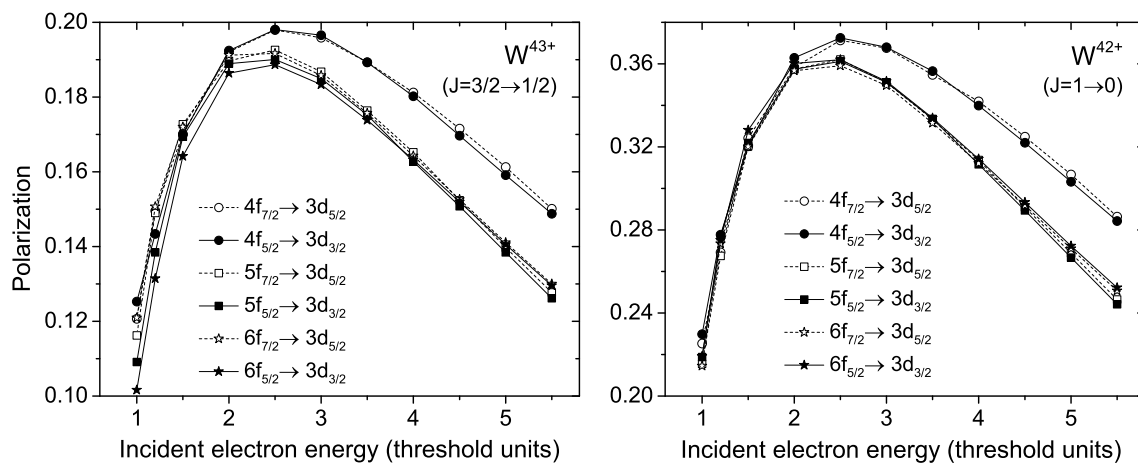
Figure 3. The presently calculated degrees of linear polarization of X-ray emissions following electron-impact excitations $3d \rightarrow nf$ ($n = 4, 5, 6$) of W^{43+} (left panel) and W^{42+} (right panel) ions as a function of incident electron energy.

Besides degrees of linear polarization of X-ray emissions following the electron-impact excitation, linear polarizations of X-ray emissions following the resonant electron capture are also studied, as shown in Table 3. It has been found that the degrees of linear polarization of these X-rays are totally different for different charged tungsten ions, compared to the case of the electron-impact excitations. For W^{45+} and W^{43+} ions, the degrees of linear polarization of all involved X-ray emissions give rise to exactly 0.6, since the cross-section $\sigma_{0 \rightarrow \pm 3/2}$ for resonant electron capture to the $M_f = 3/2$ magnetic substate is equal to zero, as discussed above. However, for W^{44+} and W^{42+} ions, they show different stories of interest. For example, the X-ray emissions from W^{44+} ions exhibit an extremely strong degree of linear polarization that reaches above 0.9. In contrast, much lesser, but still strong linearly polarized X-ray emissions are obtained for W^{42+} tungsten ions. Moreover, the linear polarizations of the $nf_{7/2} \rightarrow 3d_{5/2}$ ($n = 5, 6$) X-ray emissions are obviously stronger than the ones of the $nf_{5/2} \rightarrow 3d_{3/2}$ emissions in the case of W^{42+} and W^{44+} ions.

Table 3. The presently calculated degrees of linear polarization of X-ray emissions following resonant nf ($n = 5, 6$) electron captures of final W^{45+}–W^{42+} ions. Note that closed inner-subshells have been omitted from the initial and final levels of the radiative transitions for the sake of brevity.

Ions	Transitions	Polarization
W^{45+}	$(3d_{5/2}^{-1}4s5f_{7/2})_{J=3/2} \to (3d^{10}4s)_{J=1/2}$	0.60
	$(3d_{3/2}^{-1}4s5f_{5/2})_{J=3/2} \to (3d^{10}4s)_{J=1/2}$	0.60
	$(3d_{5/2}^{-1}4s6f_{7/2})_{J=3/2} \to (3d^{10}4s)_{J=1/2}$	0.60
	$(3d_{3/2}^{-1}4s6f_{5/2})_{J=3/2} \to (3d^{10}4s)_{J=1/2}$	0.60
W^{44+}	$(3d_{5/2}^{-1}4s^25f_{7/2})_{J=1} \to (3d^{10}4s^2)_{J=0}$	0.98
	$(3d_{3/2}^{-1}4s^25f_{5/2})_{J=1} \to (3d^{10}4s^2)_{J=0}$	0.91
	$(3d_{5/2}^{-1}4s^26f_{7/2})_{J=1} \to (3d^{10}4s^2)_{J=0}$	0.97
	$(3d_{3/2}^{-1}4s^26f_{5/2})_{J=1} \to (3d^{10}4s^2)_{J=0}$	0.89
W^{43+}	$(3d_{5/2}^{-1}4s^24p_{1/2}5f_{7/2})_{J=3/2} \to (3d^{10}4s^24p_{1/2})_{J=1/2}$	0.60
	$(3d_{3/2}^{-1}4s^24p_{1/2}5f_{5/2})_{J=3/2} \to (3d^{10}4s^24p_{1/2})_{J=1/2}$	0.60
	$(3d_{5/2}^{-1}4s^24p_{1/2}6f_{7/2})_{J=3/2} \to (3d^{10}4s^24p_{1/2})_{J=1/2}$	0.60
	$(3d_{3/2}^{-1}4s^24p_{1/2}6f_{5/2})_{J=3/2} \to (3d^{10}4s^24p_{1/2})_{J=1/2}$	0.60
W^{42+}	$(3d_{5/2}^{-1}4s^24p_{1/2}^25f_{7/2})_{J=1} \to (3d^{10}4s^24p_{1/2}^2)_{J=0}$	0.64
	$(3d_{3/2}^{-1}4s^24p_{1/2}^25f_{5/2})_{J=1} \to (3d^{10}4s^24p_{1/2}^2)_{J=0}$	0.49
	$(3d_{5/2}^{-1}4s^24p_{1/2}^26f_{7/2})_{J=1} \to (3d^{10}4s^24p_{1/2}^2)_{J=0}$	0.42
	$(3d_{3/2}^{-1}4s^24p_{1/2}^26f_{5/2})_{J=1} \to (3d^{10}4s^24p_{1/2}^2)_{J=0}$	0.23

Such huge differences in linear polarization of X-ray emissions following electron-impact excitation and resonant electron capture processes provide us a new possibility of distinguishing and identifying the population mechanism of these emissions. Further, particular plasma conditions can be also assessed by measuring linear polarization of associated X-ray emissions. For instance, electron-impact excitation would play very important roles in hot and dense plasmas, while resonant electron capture would dominate in low density plasmas that are cooled and recombining by capturing free electrons.

3.4. Dielectronic Recombination Rate Coefficients

Another part of the present work is the calculations of DR rate coefficients for highly charged tungsten ions with the purpose of tungsten plasma modeling. Before discussing these rate coefficients, we start with the comparison of DR cross-sections as shown in Figure 4 for the $3d^{10} + e^- \to 3d^94l4l' \to 3d^{10}4l'' + h\nu$ processes of W^{46+} ions to illustrate the reliability of the present calculations. A very good agreement between the present cross-sections and other available results [29] was found, especially at high electron energies. As seen from the figure, in the given electron energy range, there are many DR channels with different cross-sections, which all contribute to associated DR rate coefficients. Moreover, we also compared total DR rate coefficients of W^{37+} ions, as shown in Figure 5, with other available results from the ADAS database [76], which is being used currently for the modeling and diagnosis of

the tokamak plasmas in the fusion community. The OPEN-ADAS data are scaled from the ADPAK by adjusting empirically the recombination rates to match measurements of radiated power in the ASDEX Upgrade, while the ADAS-Type B rate coefficients are obtained from another ADAS formulation for DR, *i.e.*, Burgess Type B [51–53]. As seen from the figure, the present DR rate coefficients match the OPEN-ADAS data very well at high electron temperatures, while at low ones, the three sets of rate coefficients differ from each other. Furthermore, the present rate coefficients are similar in tendency to the results of the ADAS-Type B, but with a factor of two difference in magnitude at the electron temperatures above 2 eV. Much smaller total rate coefficients of the ADAS-Type B at low temperatures result from the omission of some configurations in the calculations [76].
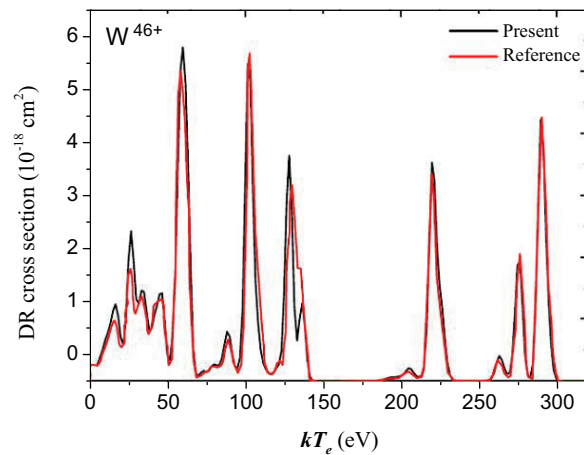

Figure 4. The presently calculated DR cross-sections for the $3d^{10} + e^- \rightarrow 3d^9 4l4l' \rightarrow 3d^{10}4l'' + h\nu$ processes of W^{46+} ions as a function of electron energy kT_e together with other available results [29].
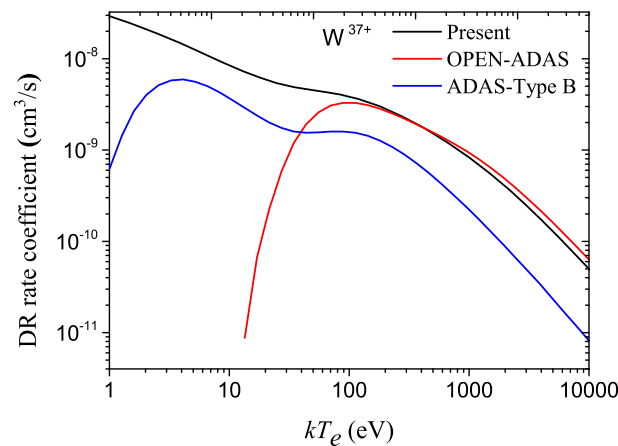
Figure 5. The presently calculated total DR rate coefficients of W^{37+} ions as a function of electron energy kT_e, compared to available ones from the ADAS database [76].

In this part, we calculate total DR rate coefficients of W^{46+}–W^{37+} ions (calculations on W^{40+} ions are currently underway). As an example, total DR rate coefficients of W^{39+} ions are displayed in Figure 6 together with their partial contributions, as associated with the $3s$, $3p$, $3d$, $4s$ and $4p$ subshell excitations as a function of electron temperature. This charge state W^{39+} is inferred to be dominant at

around 2 keV in modeling ITER plasmas [51]. The calculations of total DR rate coefficients require the summation, in principle, over an infinite number of individual level-by-level DR channels. To do this, we first calculate individual configuration-by-configuration rate coefficients, which could be achieved by performing the statistical summation over all corresponding level-by-level rate coefficients. Since the initial configuration is well defined for potentially considered DR process, the intermediate (doubly excited) and final configurations should be specified explicitly. In the case of W^{39+}, we consider the following doubly-excited configurations, $([Ne](3s^23p^63d^{10}4s^24p^5)^{-1}nln'l')^{**}$ with n = 4–8, l = 0–4, n' = 4–20 and l' = 0–12, as well as the final configurations $([Ne](3s^23p^63d^{10}4s^24p^5)^{-1}n''l''n'l')^*$ with n'' = 3–7 and l'' = 0–4 from the subsequently radiative decays. The excitations from K and L shells are not taken into account in the present calculations due to their negligible contribution to total DR rate coefficients [77]. The contributions from higher-n' states are extrapolated up to n' = 1000 using the empirical $(n')^{-3}$ scaling [78]. These rate coefficients are calculated for electron temperatures from 1 eV to 5×10^4 eV, which is a critical range for thermonuclear fusion plasmas [79]. As seen clearly from this figure, excitations from the $4p$ subshell dominate total DR rate coefficients in the whole region of electron temperature. With respect to excitations from the $3l$ subshells, it is found that the DR rate coefficients for $3d$ subshell excitation are the largest and that the partial rate coefficients decrease with the decreasing l quantum number. This characteristics is similar to the case of Sn^{12+} [77] and Pd^{19+} [80] ions. For electron temperatures lower than 100 eV, excitations from the $3l$ subshells are much less significant than from the $4l$ subshells, and thus, the contributions to total DR rate coefficients can be neglected. However, as the electron temperature increases, the $3l$ subshell excitations become more important and consequently start to compete with the $4l$ excitations. Regarding excitations from the $4l$ subshells, DR rate coefficients for the $4p$ excitation are the largest, while the contribution from the $4s$ excitation cannot be neglected. For the rest of the tungsten ions discussed above, we use the same procedures as W^{39+} ions, and very similar characteristics are summarized; thus, only total DR rate coefficients are given for them for the sake of brevity, as shown in Figure 7.
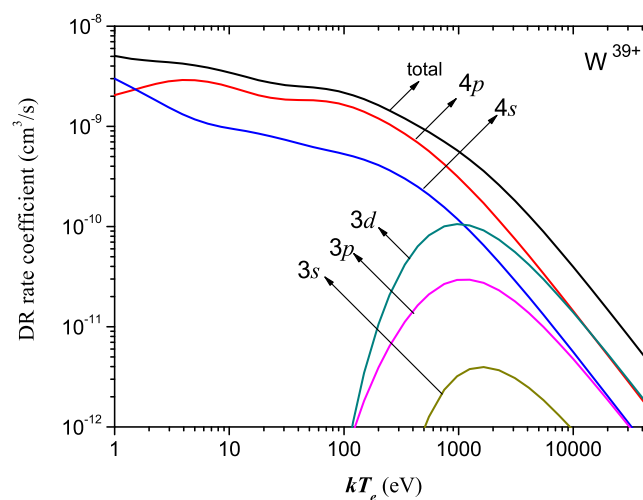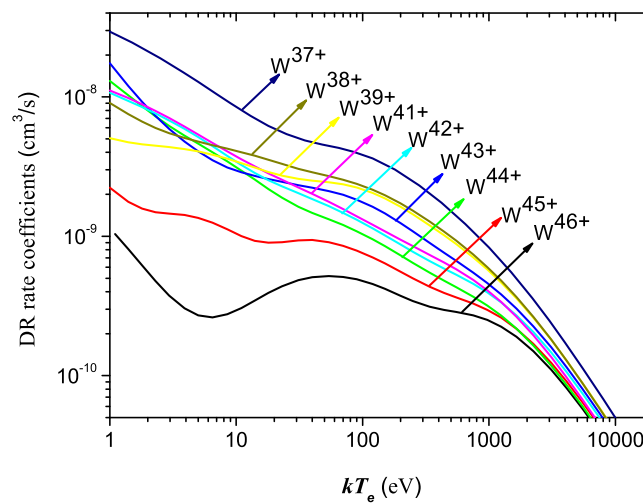

Figure 6. The presently calculated total and partial DR rate coefficients of W^{39+} ions as a function of electron temperature kT_e. This charge state W^{39+} is inferred to be dominant at around 2 keV in modeling International Thermonuclear Experimental Reactor (ITER) plasmas [51].

To facilitate the applications of DR rate coefficients, one can use the following semiempirical fitting formula (in cm$^3 \cdot$ s^{-1}) [81]:

$$\alpha^{DR}(kT_e) = \left(kT_e\right)^{-3/2} \sum_{i}^{6} A_i e^{-B_i/kT_e} . \tag{12}$$

Here, A_i and B_i are fitting parameters that can be obtained by fitting the calculated DR rate coefficients. For example, these parameters for total DR rate coefficients of W^{46+}–W^{37+} ions are listed in Table 4, which can be utilized to reproduce the presently calculated total rate coefficients with discrepancies of less than 1% for electron temperatures above 5 eV. However, one should be very careful to use the fitted data at temperatures below 5 eV, since DR rate coefficients are very sensitive to the resonance energies in that region.

Figure 7. The presently calculated total DR rate coefficients of W^{46+}–W^{37+} ions as a function of electron temperature kT_e.

Table 4. Fitting parameters for the presently calculated total DR rate coefficients of W^{46+}–W^{37+} ions. Numbers in brackets denote powers of 10.

Fitting	W^{46+}	W^{45+}	W^{44+}	W^{43+}	W^{42+}	W^{41+}	W^{39+}	W^{38+}	W^{37+}
A_1	1.4543[−8]	2.6717[−7]	1.1569[−6]	4.1371[−7]	1.6944[−6]	1.6014[−7]	6.0746[−7]	1.9070[−7]	3.9007[−7]
B_1	8.3243[0]	7.0342[0]	9.0374[1]	7.7850[0]	1.1615[2]	5.0613[0]	3.3713[1]	6.5731[0]	5.1508[0]
A_2	1.9915[−7]	4.0559[−7]	7.4592[−6]	1.6914[−6]	4.4742[−6]	4.8517[−6]	1.7700[−7]	7.7977[−7]	1.2141[−6]
B_2	4.2241[1]	3.2974[1]	7.1384[2]	5.9659[1]	3.4936[2]	3.3090[2]	6.9936[0]	3.2360[1]	3.5521[1]
A_3	6.7361[−7]	2.6009[−6]	2.5384[−7]	4.3113[−6]	6.2817[−7]	1.6915[−6]	5.7629[−6]	2.9429[−6]	5.0545[−6]
B_3	1.0717[2]	1.0912[2]	2.2324[1]	1.8934[2]	4.0746[1]	1.0235[2]	2.2787[2]	1.0602[2]	1.0896[2]
A_4	1.7027[−6]	5.9321[−6]	1.0583[−7]	9.6379[−6]	1.7999[−5]	1.2484[−5]	2.9373[−6]	6.7028[−6]	1.0545[−5]
B_4	2.7908[2]	2.7452[2]	3.8774[0]	5.9801[2]	2.1950[3]	9.1731[2]	9.8938[1]	2.5447[2]	2.4496[2]
A_5	2.0410[−5]	2.1212[−5]	2.3367[−6]	2.8462[−5]	1.7095[−7]	1.4246[−5]	2.2508[−5]	1.2033[−5]	1.5455[−5]
B_5	2.0661[3]	9.0060[2]	2.1982[2]	1.7244[3]	5.6003[0]	1.9728[3]	1.7514[3]	6.7877[2]	6.4479[2]
A_6	8.3537[−6]	4.9140[−5]	2.0007[−5]		1.4323[−5]	5.2788[−7]	1.1814[−5]	1.9456[−5]	2.1248[−5]
B_6	9.7091[2]	1.9984[3]	1.9094[3]		1.0829[3]	3.1933[1]	6.5898[2]	1.7055[3]	1.6974[3]

4. Conclusions

The degrees of linear polarization of radiated X-ray emissions following electron-impact excitation and resonant electron capture of highly charged tungsten ions have been studied. Special attention has

been focused on the strong $nf \rightarrow 3d(n = 4, 5, 6)$ M-band spectra of W^{46+}–W^{42+} ions. In order to do this, total and magnetic sub-level cross-sections for the associated excitations were discussed in much detail. It has been found that the linear polarizations of those X-rays behave very variously for different population mechanisms, even for identical transition lines. Such big differences in linear polarization of X-ray emissions following electron-impact excitation and resonant electron capture processes provide us a new possibility of distinguishing and identifying the population mechanism of these emissions. In addition, with the purpose of assisting the study and simulation of the ionization equilibrium of tungsten plasmas, DR rate coefficients of highly charged W^{37+} to W^{46+} ions are also estimated and discussed. To facilitate applications of those DR rate coefficients, a semiempirical fitting to them has been performed.

Acknowledgments

Author Contributions

Each author contributed to all aspects of the present work.

Conflicts of Interest

The authors declare no conflict of interest.

References

1. Causey, R.; Wilson, K.; Venhaus, T.; Wampler, W.R. Tritium retention in tungsten exposed to intense fluxes of 100 eV tritons. *J. Nucl. Mater.* **1999**, *266–269*, 467–471.
2. Neu, R.; Asmussen, K.; Krieger, K.; Thoma, A.; Bosch, H.-S.; Deschka, S.; Dux, R.; Engelhardt, W.; Garcia-Rosales, C.; Gruber, O.; *et al.* The tungsten divertor experiment at ASDEX Upgrade. *Plasma Phys. Control. Fus.* **1996**, *38*, A165–A179.
3. Neu, R.; Bobkov, V.; Dux, R.; Fuchs, J.C.; Gruber, O.; Herrmann, A.; Kallenbach, A.; Maier, H.; Mayer, M.; Pütterich, T.; *et al.* Ten years of W programme in ASDEX Upgrade—Challenges and conclusions. *Phys. Scr.* **2009**, *2009*, 014038.
4. Rohde, V.; Balden, M.; Lunt, T.; the ASDEX Upgrade Team. Dust investigations at ASDEX Upgrade. *Phys. Scr.* **2009**, *2009*, 014024.
5. Riccardo, V.; Firdaouss, M.; Joffrin, E.; Matthews, G.; Mertens, P.H.; Thompson, V.; Villedieu, E. Operational limits for the ITER-like wall in JET. *Phys. Scr.* **2009**, *2009*, 014033.
6. Reinke, M.L.; Beiersdorfer, P.; Howard, N.T.; Magee, E.W.; Podpaly, Y.; Rice, J.E.; Terry, J.L. Vacuum ultraviolet impurity spectroscopy on the Alcator C-Mod tokamak. *Rev. Sci. Instrum.* **2010**, *81*, 10D736.

7. Neu, R.; Dux, R.; Kallenbach, A.; Pütterich, T.; Balden, M.; Fuchs, J.C.; Herrmann, A.; Maggi, C.F.; O'Mullane, M.; Pugno, R.; *et al.* Tungsten: An option for divertor and main chamber plasma facing components in future fusion devices. *Nucl. Fus.* **2005**, *45*, 209–218.

8. Skinner, C.H. Applications of EBIT to magnetic fusion diagnostics. *Can. J. Phys.* **2008**, *86*, 285–290.

9. Reader, J. Spectral data for fusion energy: From W to W. *Phys. Scr.* **2009**, *2009*, 014023.

10. Kramida, A.E.; Shirai, T. Energy levels and spectral lines of tungsten, W III through W LXXIV. *At. Data Nucl. Data Tables* **2009**, *95*, 305–474.

11. Kramida, A.E.; Shirai, T. Erratum to "Energy levels and spectral lines of tungsten, W III through W LXXIV" [Atomic Data and Nuclear Data Tables 95 (2009) 305–474]. *At. Data Nucl. Data Tables* **2009**, *95*, 1051.

12. Kramida, A. Recent progress in spectroscopy of tungsten. *Can. J. Phys.* **2011**, *89*, 551–570.

13. Clementson, J.; Beiersdorfer, P.; Brown, G.V.; Gu, M.F.; Lundberg, H.; Podpaly, Y.; Träbert, E. Tungsten spectroscopy at the Livermore electron beam ion trap facility. *Can. J. Phys.* **2011**, *89*, 571–580.

14. Müller, A. Fusion-related ionization and recombination data for tungsten ions in low to moderately high charge states. *Atoms* **2015**, *3*, 120–161.

15. Utter, S.B.; Beiersdorfer, P.; Träbert, E. Electron-beam ion-trap spectra of tungsten in the EUV. *Can. J. Phys.* **2002**, *80*, 1503–1515.

16. Neill, P.; Harris, C.; Safronova, A.S.; Hamasha, S.; Hansen, S.; Safronova, U.I.; Beiersdorfer, P. The study of X-ray *M*-shell spectra of W ions from the Lawrence Livermore National Laboratory Electron Beam Ion Trap. *Can. J. Phys.* **2004**, *82*, 931–942.

17. Pütterich, T.; Neu, R.; Biedermann, C.; Radtke, R.; ASDEX Upgrade Team. Disentangling the emissions of highly ionized tungsten in the range 4–14 nm. *J. Phys. B* **2005**, *38*, 3071–3082.

18. Ralchenko, Y.; Tan, J.N.; Gillaspy, J.D.; Pomeroy, J.M.; Silver, E. Accurate modeling of benchmark X-ray spectra from highly charged ions of tungsten. *Phys. Rev. A* **2006**, *74*, 042514.

19. Ralchenko, Y.; Reader, J.; Pomeroy, J.M.; Tan, J.N.; Gillaspy, J.D. Spectra of W^{39+}–W^{47+} in the 12–20 nm region observed with an EBIT light source. *J. Phys. B* **2007**, *40*, 3861–3875.

20. Biedermann, C.; Radtke, R.; Seidel, R.; Pütterich, T. Spectroscopy of highly charged tungsten ions relevant to fusion plasmas. *Phys. Scr.* **2009**, *2009*, 014026.

21. Harte, C.S.; Suzuki, C.; Kato, T.; Sakaue, H.A.; Kato, D.; Sato, K.; Tamura, N.; Sudo, S.; D'Arcy, R.; Sokell, E.; *et al.* Tungsten spectra recorded at the LHD and comparison with calculations. *J. Phys. B* **2010**, *43*, 205004.

22. Fournier, K.B. Atomic data and spectral line intensities for highly ionized tungsten (Co-like W^{47+} to Rb-like W^{37+}) in a high-temperature, low-density plasma. *At. Data Nucl. Data Tables* **1998**, *68*, 1–48.

23. Safronova, U.I.; Safronova, A.S. Wavelengths and transition rates for nl-$n'l'$ transitions in Be-, B-, Mg-, Al-, Ca-, Zn-, Ag- and Yb-like tungsten ions. *J. Phys. B* **2010**, *43*, 074026.

24. Quinet, P. Dirac-Fock calculations of forbidden transitions within the $3p^k$ and $3d^k$ ground configurations of highly charged tungsten ions (W^{47+}–W^{61+}). *J. Phys. B* **2011**, *44*, 195007.

25. Quinet, P. A theoretical survey of atomic structure and forbidden transitions in the $4p^k$ and $4d^k$ ground configurations of tungsten ions W^{29+} through W^{43+}. *J. Phys. B* **2012**, *45*, 025003.

26. Loch, S.D.; Ludlow, J.A.; Pindzola, M.S.; Whiteford, A.D.; Griffin, D.C. Electron-impact ionization of atomic ions in the W isonuclear sequence. *Phys. Rev. A* **2005**, *72*, 052716.

27. Ballance, C.P.; Griffin, D.C. Relativistic radiatively damped R-matrix calculation of the electron-impact excitation of W^{46+}. *J. Phys. B* **2006**, *39*, 3617–3628.

28. Ballance, C.P.; Griffin, D.C. Electron-impact excitation of W^{44+} and W^{45+}. *J. Phys. B* **2007**, *40*, 247–258.

29. Behar, E.; Peleg, A.; Doron, R.; Mandelbaum, P.; Schwob, J.L. Dielectronic recombination of Ni-, Cu-, and Ar-like tungsten and Barium through the low inner-shell excited configurations including collision processes. *J. Quant. Spectrosc. Radiat. Transf.* **1997**, *58*, 449–469.

30. Takács, E.; Meyer, E.S.; Gillaspy, J.D.; Roberts, J.R.; Chantler, C.T.; Hudson, L.T.; Deslattes, R.D.; Brown, C.M.; Laming, J.M.; Dubau, J.; *et al.* Polarization measurements on a magnetic quadrupole line in Ne-like barium. *Phys. Rev. A* **1996**, *54*, 1342–1350.

31. Reed, K.J.; Chen, M.H. Relativistic effects on the polarization of line radiation emitted from He-like and H-like ions following electron-impact excitation. *Phys. Rev. A* **1993**, *48*, 3644–3651.

32. Fritzsche, S.; Surzhykov, A.; Stöhlker, T. Dominance of the Breit interaction in the X-ray emission of highly charged ions following dielectronic recombination. *Phys. Rev. Lett.* **2009**, *103*, 113001.

33. Hu, Z.M.; Han, X.Y.; Li, Y.M.; Kato, D.; Tong, X.M.; Nakamura, N. Experimental demonstration of the Breit interaction which dominates the angular distribution of X-ray emission in dielectronic recombination. *Phys. Rev. Lett.* **2012**, *108*, 073002.

34. Weber, G.; Bräuning, H.; Surzhykov, A.; Brandau, C.; Fritzsche, S.; Geyer, S.; Hagmann, S.; Hess, S.; Kozhuharov, C.; Märtin, R.; *et al.* Direct determination of the magnetic quadrupole contribution to the Lyman-α_1 transition in a hydrogenlike ion. *Phys. Rev. Lett.* **2010**, *105*, 243002.

35. Wu, Z.W.; Kabachnik, N.M.; Surzhykov, A.; Dong, C.Z.; Fritzsche, S. Determination of small level splittings in highly charged ions via angle-resolved measurements of characteristic X-rays. *Phys. Rev. A* **2014**, *90*, 052515.

36. Wu, Z.W.; Jiang, J.; Dong, C.Z. Influence of Breit interaction on the polarization of radiation following inner-shell electron-impact excitation of highly charged berylliumlike ions. *Phys. Rev. A* **2011**, *84*, 032713.

37. Wu, Z.W.; Dong, C.Z.; Jiang, J. Degrees of polarization of the two strongest $5f \rightarrow 3d$ lines following electron-impact excitation and dielectronic recombination processes of Cu-like to Se-like gold ions. *Phys. Rev. A* **2012**, *86*, 022712.

38. Jiang, J.; Dong, C.Z.; Xie, L.Y.; Wang, J.G. Resonance electron-impact excitation and polarization of the magnetic quadrupole line of neonlike Ba^{46+} ions. *Phys. Rev. A* **2008**, *78*, 022709.

39. Schippers, S.; Bernhardt, D.; Müller, A.; Krantz, C.; Grieser, M.; Repnow, R.; Wolf, A.; Lestinsky, M.; Hahn, M.; Novotný, O.; *et al.* Dielectronic recombination of xenonlike tungsten ions. *Phys. Rev. A* **2011**, *83*, 012711.

40. Spruck, K.; Badnell, N.R.; Krantz, C.; Novotný, O.; Becker, A.; Bernhardt, D.; Grieser, M.; Hahn, M.; Repnow, R.; Savin, D.W.; *et al.* Recombination of W^{18+} ions with electrons: Absolute rate coefficients from a storage-ring experiment and from theoretical calculations. *Phys. Rev. A* **2014**, *90*, 032715.

41. Ballance, C.P.; Loch, S.D.; Pindzola, M.S.; Griffin, D.C. Dielectronic recombination of W^{35+}. *J. Phys. B* **2010**, *43*, 205201.

42. Badnell, N.R.; Ballance, C.P.; Griffin, D.C.; O'Mullane, M. Dielectronic recombination of W^{20+} ($4d^{10}4f^8$): Addressing the half-open f shell. *Phys. Rev. A* **2012**, *85*, 052716.

43. Dzuba, V.A.; Flambaum, V.V.; Gribakin, G.F.; Harabati, C. Chaos-induced enhancement of resonant multielectron recombination in highly charged ions: Statistical theory. *Phys. Rev. A* **2012**, *86*, 022714.

44. Dzuba, V.A.; Flambaum, V.V.; Gribakin, G.F.; Harabati, C.; Kozlov, M.G. Electron recombination, photoionization, and scattering via many-electron compound resonances. *Phys. Rev. A* **2013**, *88*, 062713.

45. Safronova, U.I.; Safronova, A.S.; Beiersdorfer, P. Dielectronic recombination of Rh-like Gd and W. *Phys. Rev. A* **2012**, *86*, 042510.

46. Ralchenko, Y.; Gillaspy, J.D. Anisotropic *LMN* dielectronic resonances from ratios of magnetic-dipole lines. *Phys. Rev. A* **2013**, *88*, 012506.

47. Li, B.W.; O'Sullivan, G.; Fu, Y.B.; Dong, C.Z. Dielectronic recombination of Rh-like Gd and W. *Phys. Rev. A* **2012**, *85*, 052706.

48. Li, M.J.; Fu, Y.B.; Su, M.G.; Dong, C.Z.; Koike, F. Dielectronic recombination of Br-Like tungsten ions. *Plasma Sci. Technol.* **2014**, *16*, 182–187.

49. Li, M.J.; Fu, Y.B.; Zhang, G.D.; Zhang, Y.Z.; Dong, C.Z.; Koike, F. Dielectronic recombination of the 4p and 4d open sub-shell tungsten ions. *J. Phys.* **2014**, *488*, 062022.

50. Wu, Z.W.; Zhang, Y.Z.; Fu, Y.B.; Surzhykov, A.; Fritzsche, S.; Dong, C.Z. Dielectronic recombination rate coefficients of initially rubidium-like tungsten. *Eur. Phys. J. D* **2015**, *69*, 140.

51. Pütterich, T.; Neu, R.; Dux, R.; Whiteford, A.D.; O'Mullane, M.G.; the ASDEX Upgrade Team. Modelling of measured tungsten spectra from ASDEX Upgrade and predictions for ITER. *Plasma Phys. Control. Fus.* **2008**, *50*, 085016.

52. Summers, H.P. The ADAS User Manual, Version 2.6, 2004. Available online: http://www.adas.ac.uk (accessed on 10 November 2015)

53. Badnell, N.R.; O'Mullane, M.G.; Summers, H.P.; Altun, Z.; Bautista, M.A.; Colgan, J.; Gorczyca, T.W.; Mitnik, D.M.; Pindzola, M.S.; Zatsarinny, O. Dielectronic recombination data for dynamic finite-density plasmas I. Goals and methodology. *Astron. Astrophys.* **2003**, *406*, 1151–1165.

54. Burgess, A. A general formula for the estimation of dielectronic recombination coefficients in low-density plasmas. *Astrophys. J.* **1965**, *141*, 1588–1590.

55. Trzhaskovskaya, M.B.; Nikulin, V.K.; Clark, R.E.H. Radiative recombination rate coefficients for highly-charged tungsten ions. *At. Data Nucl. Data Tables* **2010**, *96*, 1–25.

56. Trzhaskovskaya, M.B.; Nikulin, V.K. Radiative recombination data for tungsten ions: I. W^{24+}–W^{45+}. *At. Data Nucl. Data Tables* **2013**, *99*, 249–311.

57. Trzhaskovskaya, M.B.; Nikulin, V.K. Radiative recombination data for tungsten ions: II. W^{47+}–W^{71+}. *At. Data Nucl. Data Tables* **2014**, *100*, 986–1058.

58. Trzhaskovskaya, M.B.; Nikulin, V.K. Radiative recombination data for tungsten ions: III. W^{14+}–W^{23+}. *At. Data Nucl. Data Tables* **2014**, *100*, 1156–1188.

59. Jiang, J.; Dong, C.Z.; Xie, L.Y.; Wang, J.G.; Yan, J.; Fritzsche, S. Relativistic distorted-wave calculations of electron impact excitation cross-sections of Be-like C^{2+} ions. *Chin. Phys. Lett.* **2007**, *24*, 691–694.

60. Zhang, H.L.; Sampson, D.H.; Clark, R.E.H. Relativistic cross-sections for excitation of highly charged ions to specific magnetic sub-levels by an electron beam. *Phys. Rev. A* **1990**, *41*, 198–206.

61. Zhang, H.L.; Sampson, D.H. Resonance contributions to collision strengths for transitions between magnetic sub-levels in highly charged ions by impact with an electron beam. *Phys. Rev. A* **2002**, *66*, 042704.

62. Parpia, F.A.; Fischer, C.F.; Grant, I.P. GRASP92: A package for large-scale relativistic atomic structure calculations. *Comput. Phys. Commun.* **1996**, *94*, 249–271.

63. Fritzsche, S. The RATIP program for relativistic calculations of atomic transition, ionization and recombination properties. *Comput. Phys. Commun.* **2012**, *183*, 1525–1559.

64. Percival, I.C.; Seaton, M.J. The polarization of atomic line radiation excited by electron impact. *Philos. Trans. R. Soc. Lond. Ser. A* **1958**, *251*, 113–138.

65. Blum, K. *Density Matrix Theory and Applications*; Plenum: New York, NY, USA, 1981.

66. Balashov, V.V.; Grum-Grzhimailo, A.N.; Kabachnik, N.M. *Polarization and Correlation Phenomena in Atomic Collisions*; Kluwer Academic: New York, NY, USA, 2000.

67. Xie, L.Y.; Ma, X.Y.; Dong, C.Z.; Wu, Z.W.; Shi, Y.L.; Jiang, J. Polarization of the $nf \rightarrow 3d$ ($n = 4, 5, 6$) X-rays from tungsten ions following electron-impact excitation and dielectronic recombination processes. *J. Quant. Spectrosc. Radiat. Transfer* **2014**, *141*, 31–39.

68. Dubau, J.; Volonté, S. Dielectronic recombination and its applications in astronomy. *Rep. Prog. Phys.* **1980**, *43*, 199–251.

69. Gu, M.F. Dielectronic recombination rate coefficients for H-like through Ne-like isosequences of Mg, Si, S, Ar, Ca, Fe, and Ni. *Astrophys. J.* **2003**, *590*, 1131–1140.

70. Gu, M.F. The flexible atomic code. *Can. J. Phys.* **2008**, *86*, 675–689.

71. Clementson, J. *Spectroscopic Investigations of Highly Charged Tungsten Ions—Atomic Spectroscopy and Fusion Plasma Diagnostics*; Atomic Physics Division, Department of Physics, Lund University: Lund, Sweden, 2010.

72. Das, T.; Sharma, L.; Srivastava, R. Electron impact excitation of the M-shell electrons from Zn-like through Co-like tungsten ions. *Phys. Scr.* **2012**, *86*, 035301.

73. Clementson, J.; Beiersdorfer, P.; Brown, G.V.; Gu, M.F.; Spectroscopy of M-shell X-ray transitions in Zn-like through Co-like W. *Phys. Scr.* **2010**, *81*, 015301.

74. Zhang, H.L.; Sampson, D.H.; Fontes, C.J. Relativistic distorted-wave collision strengths and oscillator strengths for the 33 Ni-like ions with $60 \leq Z \leq 92$. *At. Data Nucl. Data Tables* **1991**, *48*, 91–163.

75. Nakamura, N.; Kavanagh, A.P.; Watanabe, H.; Sakaue, H.A.; Li, Y.M.; Kato, D.; Currell, F.J.; Ohtani, S. Evidence for strong Breit interaction in dielectronic recombination of highly charged heavy ions. *Phys. Rev. Lett.* **2008**, *100*, 073203.

76. O'Mullane, M.G. (Department of Physics, University of Strathclyde, Glasgow, UK). Private communication, 2015.

77. Fu, Y.B.; Dong, C.Z.; Su, M.G.; Koike, F.; O'Sullivan, G.; Wang, J.G. Theoretical investigation of dielectronic recombination of Sn^{12+} ions. *Phys. Rev. A* **2011**, *83*, 062708.

78. Safronova, U.; Kato, T.; Ohira, M. Dielectronic recombination rate coefficients to the excited states of CIII from CIV. *J. Quant. Spectrosc. Radiat. Transfer* **1997**, *58*, 193–215.

79. Clark, R.E.H.; Reiter, D.H. *Nuclear Fusion Research*; Springer: New York, NY, USA, 2005.

80. Zhang, H.; Li, Y.M.; Yan, J.; Wang, J.G. Dielectronic recombination processes through doubly excited states $(4l4l', 4l5l')$ in Co-like Pd ions. *Phys. Rev. A* **2005**, *71*, 042705.

81. Meng, F.C.; Chen, C.Y.; Wang, Y.S.; Zou, Y.M. Total dielectronic recombination rate coefficient for Co-like tungsten. *J. Quant. Spectrosc. Radiat. Transfer* **2008**, *109*, 2000–2008.